materials

MDPI

Article

Mo_3Ni_2N Nanoparticle Generation by Spark Discharge

Jonas Elmroth Nordlander [1], Marie Bermeo [2], Pau Ternero [2], David Wahlqvist [3], Toni Schmeida [4], Sara Blomberg [1], Maria E. Messing [2], Martin Ek [3] and Julia-Maria Hübner [3,*]

[1] Department of Chemical Engineering and NanoLund, Lund University, P.O. Box 124, 22100 Lund, Sweden
[2] Department of Physics and NanoLund, Lund University, P.O. Box 118, 22100 Lund, Sweden
[3] Department of Chemistry and NanoLund, Lund University, P.O. Box 124, 22100 Lund, Sweden
[4] Leibniz-Institut für Festkörper- und Werkstoffforschung, Helmholtzstraße 20, 01069 Dresden, Germany
* Correspondence: julia-maria.hubner@chem.lu.se

Abstract: Spark ablation is an advantageous method for the generation of metallic nanoparticles with defined particle sizes and compositions. The reaction of the metal particles with the carrier gas during the synthesis and, therefore, the incorporation of those light elements into structural voids or even compound formation was confirmed for hydrides and oxides but has only been suspected to occur for nitrides. In this study, dispersed nanoparticles of Mo_3Ni_2N and Mo with Janus morphology, and defined particle sizes were obtained by spark discharge generation as a result of carrier gas ionization and characterized using transmission electron microscopy and powder X-ray diffraction. Metal nitrides possess beneficial catalytic and thermoelectric properties, as well as high hardness and wear resistance. Therefore, this method offers the possibility of controlled synthesis of materials which are interesting for numerous applications.

Keywords: metal nitrides; nanoparticles; spark discharge; carrier gas

Citation: Elmroth Nordlander, J.; Bermeo, M.; Ternero, P.; Wahlqvist, D.; Schmeida, T.; Blomberg, S.; Messing, M.E.; Ek, M.; Hübner, J.-M. Mo_3Ni_2N Nanoparticle Generation by Spark Discharge. *Materials* **2023**, *16*, 1113. https://doi.org/10.3390/ma16031113

Academic Editor: Enrico Negro

Received: 7 December 2022
Revised: 19 January 2023
Accepted: 24 January 2023
Published: 27 January 2023

1. Introduction

Metal nitrides are a class of ceramic materials possessing a number of beneficial properties, including excellent mechanical robustness due to their high hardness and wear resistance [1,2], high chemical stability, and electrical conductivity [3]. Their outstanding properties make metal nitrides suitable for a broad range of technological applications. For instance, BN is an important high-temperature ceramic material, whereas group 13 nitrides (AlN, GaN, InN) are used in opto- and microelectronic devices [4,5]. In thermoelectric materials, nitride inclusions can act as phonon scattering centers, resulting in reduced thermal conductivity and, therefore, in a higher figure of merit [6,7]. Furthermore, transition metal nitrides are of interest as cost-efficient alternatives compared to group VIII noble metals in diverse reactions, especially those involving heterogeneous catalysts [8–10], due to their similar electrocatalytic activity but without the downside of deactivation and poisoning [11]. Recently, the ternary nitride Mo_3Ni_2N was found to be an outstanding catalyst both for oxygen [12] and hydrogen evolution [13,14].

In general, the synthesis of metal nitrides can be achieved by a wide variety of strategies in accordance with the anticipated application, starting with classical methods including direct nitridation of the elements at high temperatures, thermal decomposition of metal amides, or the reduction of metal halides or oxides in the presence of nitrogen gas (for an extensive review of preparation techniques, see [15]). Nevertheless, heterogeneous catalysis requires high surface areas as one of the critical parameters determining the reaction rate [16]. The application of ammonolysis of different precursor compounds is one of the most widely used techniques to achieve a suitable morphology. However, heat management issues during synthesis [17], as well as various side products, poor crystallinity, or different particle sizes and shapes in the resulting products are often encountered. In contrast, spark discharge generation offers the possibility of size-selective synthesis of nanoparticles

with defined particle concentrations [18]. With this method, Mo_3Al_2C-type (filled β-Mn structure) Mo_3Ni_2N nanoparticles were obtained. The nanoparticles were characterized using powder X-ray diffraction, transmission electron microscopy, and energy-dispersive X-ray spectroscopy.

2. Materials and Methods

2.1. Preparation

Nanoparticles were synthesized by spark discharge generation (for a detailed description of the method, see [18]). Ni or $Ni_{30}Mo_{70}$ rods (3 mm diameter) served as capacitor electrodes. The distance between the electrodes was kept constant, with a separation of 1.5 mm. N_2 with 5% H_2 was used as a carrier gas to avoid oxidation during particle formation [19]. Compaction of the particles was carried out at 1200 °C. The mobility diameter was set for size-selected particles to 30 nm with a differential mobility analyzer (DMA) located after the compaction furnace. For both size- and non-size-selected particles, the process was followed by deposition onto suitable substrates which were chosen according to the subsequent characterization method. Oxidization of the nanoparticles was performed in a muffle furnace at 400, 510, and 600 °C in air. For size-selected samples, a heating rate of 5 °C/min, followed by annealing for 5 min at the target temperature, and cooling with a rate of 15 °C/min were applied. For non-size-selected samples, a heating rate of 1 °C/min and a cooling rate of 15 °C/min were used.

2.2. Powder X-ray Diffraction (PXRD)

For PXRD samples, compacted particles were deposited on 4 × 4 or 5 × 5 mm SiO_x wafers (Siegert Wafer, J12004, lot no. 317559) without size selection to improve the deposition rate. The samples were transferred from the Si wafers to scotch tape, which was then loaded into the diffraction set-up. PXRD measurements were carried out in transmission mode using a STOE STADI MP X-ray diffractometer (Mythen 1k detector, Cu-K_α radiation, λ = 1.54178 Å).

2.3. Transmission Electron Microscopy (TEM)

Size-selected particle samples were created by directly depositing particles onto amorphous SiN grids (PELCO Prod. No. 21569CL-10, Batch CLEM-ULS-SN-MOS-A010(9)-T200-015_BL22) at a surface concentration of 90 μm^{-2}. To characterize non-size selected samples (as-cast, see Table S1), particles from the SiO_x wafers as described for PXRD were transferred onto lacey carbon Cu grids by gently moving the grids across the sample surface. High-resolution imaging and energy-dispersive X-ray spectroscopy (EDX) mapping were carried out using a JEOL 3000F TEM (300 kV accelerating voltage) with an Oxford Instruments X-max 80 mm^2 detector. EDX maps were acquired in scanning TEM (STEM) mode, using high-angle annular darkfield (HAADF) imaging to identify suitably oriented particles, and processed using routines from the HyperSpy [20] Python library. Curve-fitting was first carried out on the sum spectrum from the spectrum image to evaluate a fixed background model and characteristic X-ray peaks for each element (fixing energy and weightings). The spectrum image was then convoluted with a Gaussian filter (σ = 2 pixels) [21] before performing a linear fit of the previously determined peaks to the individual pixels. The corresponding maps, therefore, include contributions from all relevant peak families for each element. Standardless quantification of EDX spectra was conducted using the program INCA (Oxford Instruments). The simulation of EDX spectra was performed using the software DTSA-II [22,23]. Electron energy-loss spectroscopy (EELS) mappings were carried out using a probe-corrected FEI Titan TEM operated at 300 kV. The convergence and collection semi-angles were 22 and 56.5 mrad, respectively. The spectrometer dispersion was 0.5 eV, and the spectral range was 150–1175 eV.

3. Results and Discussion

Bimetallic Ni-Mo nanoparticles with defined particle surface concentrations are synthesized by spark discharge generation (Table S1). By employing an integrated filtering system in the spark ablation system, particles with defined diameters of 30 nm are obtained (Figure 1a; note that a larger-than-usual particle is included in this overview image and is used for further analysis at higher resolution because it happened to be aligned close to the zone axis for the Ni-Mo phase).

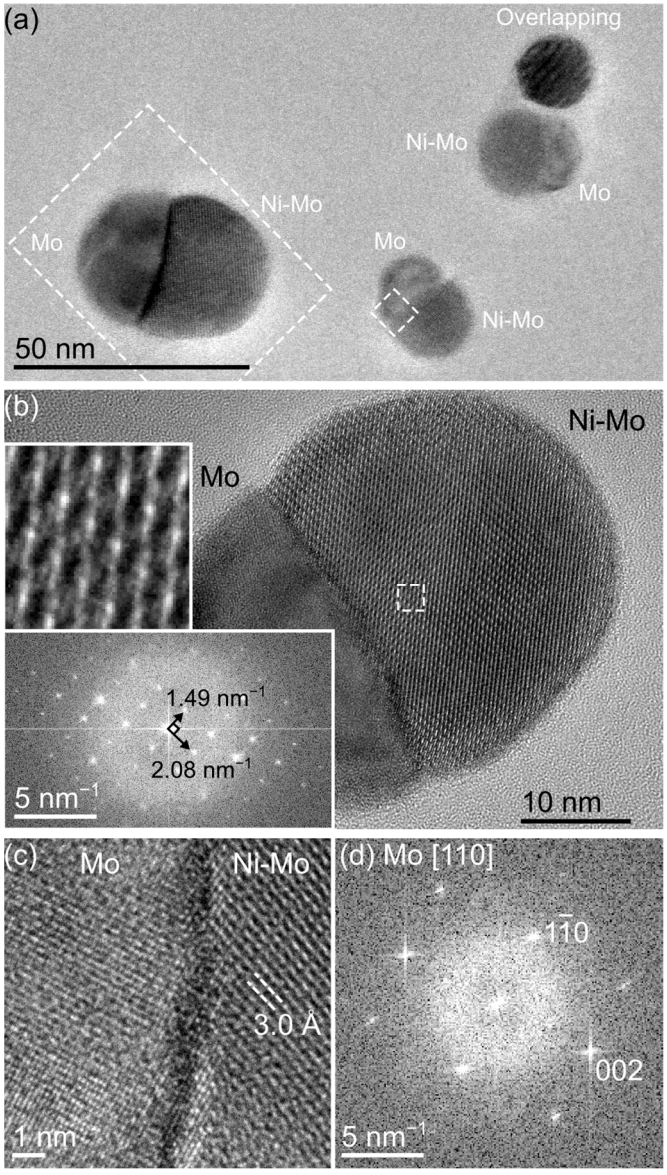

Figure 1. (**a**) Overview of an as-deposited Ni-Mo sample on an amorphous SiN substrate. The two phases are indicated for each particle. The marked regions are shown in more detail in subsequent panels. (**b**) HR-TEM image of the larger particle marked in (**a**), with insets showing the phase contrast pattern from a 2.5 × 2.5 nm^2 region and corresponding diffractogram from the Ni-Mo phase (corresponding to the [001] zone of Mo_3Ni_2N, as described later). (**c**) HR-TEM image showing the interface between the two phases from the smaller particle marked in (**a**). The pure Mo phase shows lattice spacings corresponding to pure *bcc* Mo in a [110] viewing direction, as further shown by the diffractogram in (**d**) (excluding the Ni-Mo phase).

As-deposited samples predominantly contain biphasic particles exhibiting a Janus morphology with two distinct halves (Figure 1b). The first phase can be easily identified

based on HR-TEM images (Figure 1c,d) and STEM-EDX mapping (Figure 2) as elemental Mo. The second phase contains both Ni and Mo with a Ni:Mo ratio estimated by EDX to be 35:65. Furthermore, the EDX maps indicate that the bimetallic phase has incorporated N (Figure 2b). Simulated EDX spectra (Figure S1) and complementary EELS analysis (Figure S2) confirm the presence of N and the reliability of the EDX mapping. The level of N incorporation can, however, not be determined by either EDX (due to low signal from light elements) or EELS (due to overlap with Mo edges [24], which also prevents reliable mapping of the N distribution with this technique).

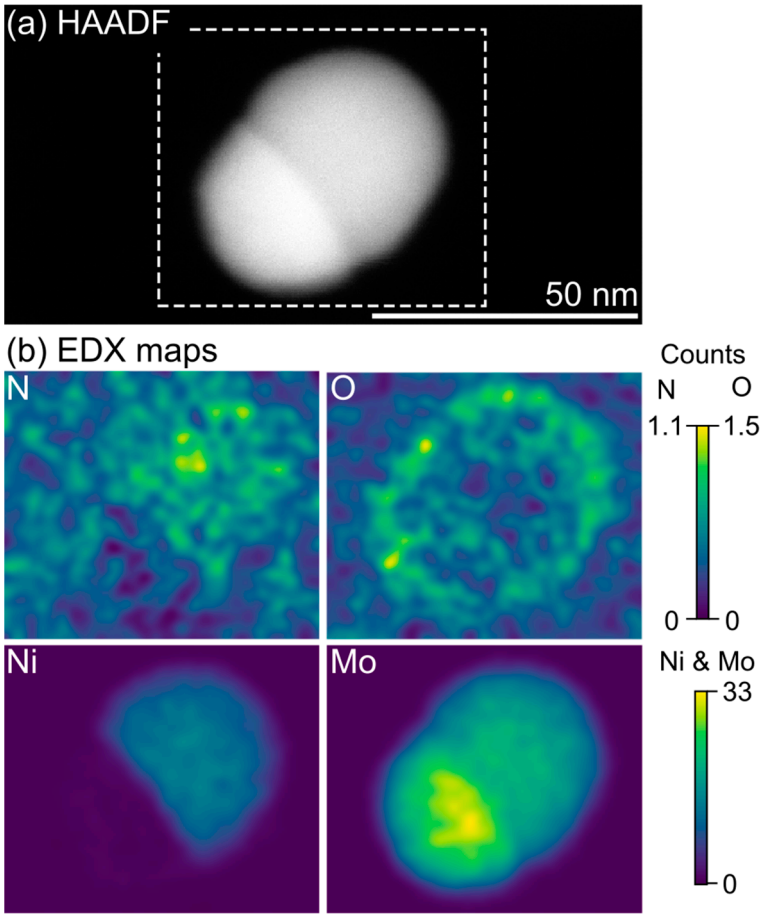

Figure 2. (**a**) STEM-HAADF overview image of a biphasic particle exhibiting a Janus morphology. (**b**) EDX mapping of the particle shows one phase containing elemental Mo (lower half) and the other containing an Ni-Mo compound with an increased N signal (upper half). Due to sample transfer being conducted in ambient air, the particles have a thin, oxidized shell.

Identification and detailed characterization of the bimetallic phase require the application of PXRD (Figure 3). PXRD revealed Mo_3Ni_2N in addition to elemental Mo (Figure 3). Mo_3Ni_2N crystallizes in the cubic space group $P4_132$ and is isotypic to Mo_3Al_2C (filled β-Mn structure), with the lattice parameter a = 6.6394(1) Å. The unit cell dimensions are in accordance with high-resolution TEM images and selected area electron diffraction along the [001] zone axis (Figure 1b). The unit cell dimensions are in good agreement (difference of the lattice parameters <1%) with previous reports of Mo_3Ni_2N synthesized by ammonolysis [25] or by reduction–nitridation of $NiMoO_4$ or mixed metal powders [26].

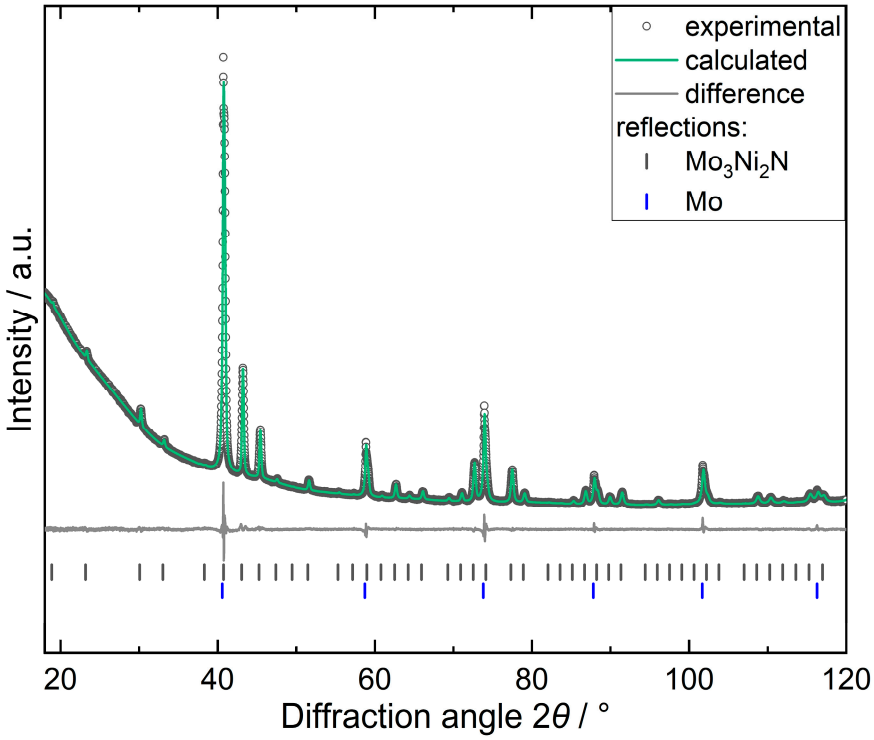

Figure 3. Rietveld refinement of Mo_3Ni_2N.

Rietveld refinement results in residuals $R = 0.0169$ and $wR = 0.0198$ (Table 1), which are lower than previous refinements comprising residuals $R = 0.1107$, $wR = 0.1590$ [25], and $wRp = 0.0634$ [26]. Therefore, the presented model provides an improved fit to the data. Both positional and displacement parameters were allowed to refine freely. All sites are fully occupied, and the displacement ellipsoids of Mo, Ni, and N are close to being spherical (Table 2).

Table 1. X-ray diffraction data for Mo_3Ni_2N. Further details on the crystal structure investigations can be obtained from the Fachinformationszentrum Karlsruhe, 76344 Eggenstein-Leopoldshafen, Germany (email: crysdata@fiz-karlsruhe.de, https://www.ccdc.cam.ac.uk/structures/? (accessed on 6 December 2022)) on quoting the depository numbers CSD-2218820.

Composition	Mo_3Ni_2N
Space group, Pearson symbol	$P4_132$ (No. 213), $cP24$
Unit cell parameters	
a [Å]	6.6394(1)
V [Å^3]	292.67(1)
Formula units Z	4
Diffractometer	Stoe Stadi MP, Mythen 1k detector, Cu-Kα radiation, $\lambda = 1.5406$ Å, transmission mode
Measurement range, 2θ step	$16.535 \leq 2\theta \leq 121.085$, $\Delta 2\theta = 0.015$
Measured points/reflections	7740/46
Residuals and GOF	$R = 0.0169$, $wR = 0.0198$, GOF = 2.1451

Table 2. Position and displacement parameters for Mo_3Ni_2N.

Atom	Site	*a*/x	*b*/y	*c*/z	$U_{iso/aniso}$
Mo	*12d*	1/8	0.2019(1)	0.4519(1)	0.0075(2)
Ni	*8c*	0.0675(1)	0.0675(1)	0.0675(1)	0.0045(2) *
N	*4a*	3/8	3/8	3/8	0.010(2)

* $U_{11} = U_{22} = U_{33} = 0.0045(3)$; $U_{12} = U_{13} = -0.0006(4)$; $U_{23} = 0.0006(4)$.

In Mo_3Ni_2N, N occupies the octahedral voids of a β-Mn type structure and is surrounded solely by Mo (Figure 4). The octahedral voids form a corner-sharing network. The coordination number of Mo is 14, and that of Ni is 12. The interatomic distances for Mo-N and Mo-Ni are in line with those of other Mo nitrides [27,28] and Mo-Ni compounds [29], respectively (Table 3). Interestingly, the homoatomic distances for Mo-Mo and Ni-Ni (Table 3) are very similar to the ones observed in the respective elements (deviation < 2%, [30,31]).

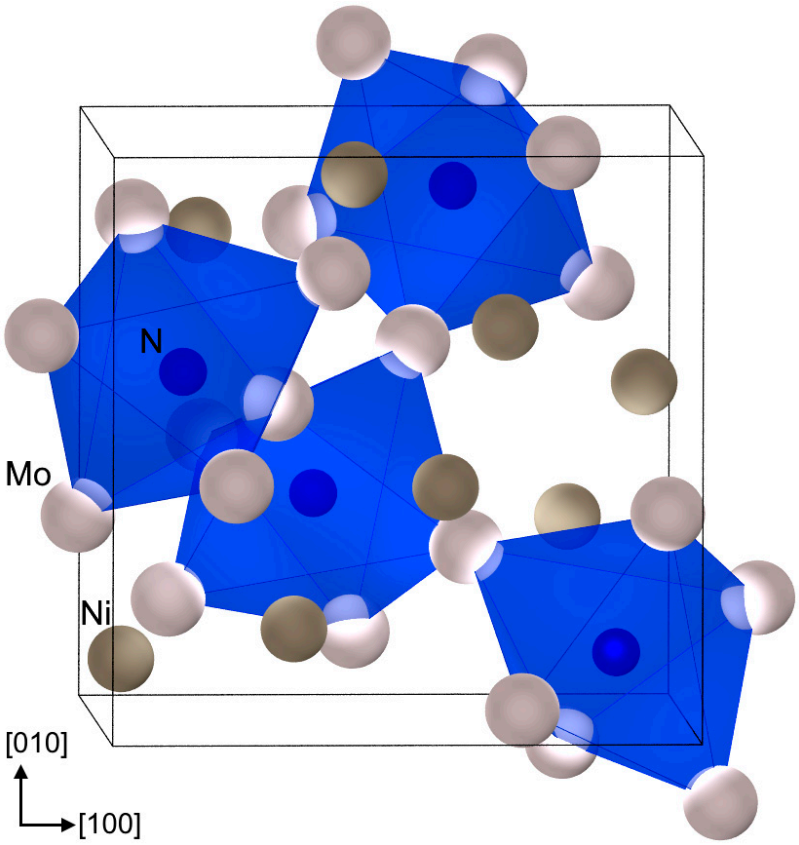

Figure 4. Crystal structure of Mo_3Ni_2N with corner-sharing distorted octahedra centered by N.

Table 3. Selected interatomic distances in Mo_3Ni_2N.

Atoms		Distance/Å	Atoms		Distance/Å
Mo	2 N	2.0825(2)	Ni	3 Ni	2.469(1)
	2 Ni	2.7309(9)		3 Mo	2.7309(9)
	2 Ni	2.7459(9)		3 Mo	2.7459(9)
	4 Mo	2.7796(4)		3 Mo	2.8206(9)
	2 Mo	2.8153(5)			
	2 Ni	2.8206(9)	N	8 Mo	2.0825(2)

The overall Ni:Mo ratio in the biphasic nanoparticles is in good agreement with the initial electrode composition, as expected in the case of alloyed electrodes [32]. By PXRD, elemental Mo is observed and refined to a phase fraction of 47.5%. However, due to the very strong overlap of all observed Mo peaks with the primary phase, the accuracy of this result is expected to be very limited. EDX measurements instead provide more precise measurements from isolated particles (both in size-selected samples as well as for similar-size particles selected from non-size-selected samples). Here, an overall Mo fraction of 70% $\pm$ 5 at.-% Mo is observed (Table S2). These measurements are further complemented by analysis of the TEM images where the composition is estimated by assuming the two phases have spherical cap morphologies (Figure S3). In line with the EDX measurement and electrode composition, the image analysis yields a Mo fraction of 73% $\pm$ 2 at.-% (Table S3).

The Mo_3Ni_2N nanoparticles generated by spark discharge are stable and show good resilience toward oxidation. Storage in ambient air results only in a thin surface oxide layer, visible in the EDX maps (Figure 2b) but not identifiable as a separate crystalline surface phase in the HR-TEM images (Figure 1b). This surface layer appears self-limiting and does not increase measurably in thickness even after six months of storage (Figure S2). Heat treatment of the samples leads to the decomposition of the nitride compound and the formation of binary and ternary oxides (Table S1) in accordance with previous studies [25].

Whereas several examples of the formation of, e.g., hydrides and oxides by spark discharge generation [33–37] are known, the possibility of nitride formation as a result of carrier gas ionization during spark discharge generation was under discussion but not validated hitherto. In contrast, the methodologically related laser ablation synthesis was employed, e.g., to obtain aluminum nitride nanoparticles [38]. Spark discharge generation offers the opportunity for straightforward synthesis of metal nitride nanoparticles in addition to other established methods [39].

As mentioned above, the obtained nanoparticles show a Janus morphology with two distinct halves. The first half consists of Mo_3Ni_2N, which is of special interest as a heterogeneous catalyst [8–10] both for oxygen [12] and hydrogen evolution [13,14]. Molybdenum, present in the second half, was reported to act as an effective catalytic promoter either in the elemental form [40] or as oxide [41] or sulfide [42], potentially accessible after further sample treatment. The possibility of enhancement of the catalytic activity of Mo_3Ni_2N by the presence of Mo or further reaction products will be subject to future studies.

4. Conclusions

Nanoparticles with a Janus morphology of the nitride Mo_3Ni_2N and elemental Mo were obtained by spark discharge generation due to carrier gas ionization. The method offers the possibility of synthesizing well-dispersed nanoparticles with defined particle sizes. Therefore, further application to other technically relevant intermetallic systems has the potential for straightforward synthesis of high-quality nanocrystalline nitrides.

Supplementary Materials: The following supporting information can be downloaded at: https://www.mdpi.com/article/10.3390/ma16031113/s1, Figure S1: STEM-EDX map; Figure S2: STEM-HAADF images and EEL spectra; Figure S3: Measurement scheme for particle volume calculation; Table S1: Synthesis conditions; Table S2: Particle composition; Table S3: Mo content in isolated particles. CCDC 2218820 contains the supplementary crystallographic data for this paper. These data can be obtained free of charge via https://www.ccdc.cam.ac.uk/structures/? (accessed on 6 December 2022), or by emailing data_request@ccdc.cam.ac.uk, or by contacting The Cambridge Crystallographic Data Centre, 12 Union Road, Cambridge CB2 1EZ, UK; Fax: +44-1223-336033.

Author Contributions: Conceptualization, M.E.M., M.E. and J.-M.H.; software, J.E.N., T.S., M.E. and J.-M.H.; investigation, J.E.N., M.B., P.T., D.W., M.E. and J.-M.H.; resources, S.B., M.E.M. and M.E.; data curation, M.E. and J.-M.H.; writing—original draft preparation, J.E.N., M.E. and J.-M.H.; writing—review and editing, M.E. and J.-M.H.; visualization, J.E.N., M.E. and J.-M.H.; supervision, M.E.M., M.E. and J.-M.H. All authors have read and agreed to the published version of the manuscript.

Funding: This research received financial support from NanoLund. The contributions by D. Wahlqvist and M. Ek were funded by the Swedish Research Council (VR), grant number 2017-04902, and the contributions by M. E. Messing, M. Bermeo, and P. Ternero were funded by the European Union's H2020 MSCA (Grant No. 945378) (GenerationNano), the Swedish Research Council (Grant No. 2019-04970), and the Swedish Foundation for Strategic Research (Grant No. FFL18-0282). The access to ARTEMI, the Swedish national infrastructure of advanced electron microscopy, was funded by the Swedish Research Council (VR), grant number 2021-00171, and the Swedish Foundation for Strategic Research (SSF), grant number RIF21-0026. Part of the experimental work was performed in the Lund Nano Lab, part of the Myfab research infrastructure.

Institutional Review Board Statement: Not applicable.

Informed Consent Statement: Not applicable.

Data Availability Statement: CCDC 2218820 contains the supplementary crystallographic data for this paper. These data can be obtained free of charge via https://www.ccdc.cam.ac.uk/structures/? (accessed on 6 December 2022), or by emailing data_request@ccdc.cam.ac.uk, or by contacting The Cambridge Crystallographic Data Centre, 12 Union Road, Cambridge CB2 1EZ, UK; Fax: +44-1223-336033.

Acknowledgments: J. Palisaitis is acknowledged for performing the EELS measurements.

Conflicts of Interest: The authors declare no conflict of interest.

References

1. Oyama, S.T. *The Chemistry of Transition Metal Carbides and Nitrides*; Blackie Academic & Professional: Glasgow, UK, 1996.
2. Toth, L.E. *Transition Metal Carbides and Nitrides*; Academic Press: New York, NY, USA, 1971.
3. Wang, H.; Li, J.; Li, K.; Lin, Y.; Chen, J.; Gao, L.; Nicolosi, V.; Xiao, X.; Lee, J.-M. Transition metal nitrides for electrochemical energy applications. *Chem. Soc. Rev.* **2021**, *50*, 1354–1390. [CrossRef] [PubMed]
4. Naik, G.; Kim, J.; Kinsey, N.; Boltasseva, A. Alternative Plasmonic Materials. In *Handbook of Surface Science*; Richardson, N.V., Holloway, S., Eds.; Elsevier: Amsterdam, The Netherlands, 2014; Chapter 6; Volume 4, pp. 189–221. [CrossRef]
5. Rao, C.N.R.; Ghosh, A.; Gomathi, A. Functionalization and Solubilization of Carbon and Inorganic Nanostructures. In *Comprehensive Nanoscience and Technology*; Andrews, D.L., Scholes, G.D., Wiederrecht, G.P., Eds.; Academic Press: Cambridge, MA, USA, 2011; pp. 445–490. [CrossRef]
6. Gomell, L.; Haeger, T.; Roscher, M.; Bishara, H.; Heiderhoff, R.; Riedl, T.; Scheu, C.; Gault, B. Microstructure manipulation by laser-surface remelting of a full-Heusler compound to enhance thermoelectric properties. *Acta Mater.* **2022**, *223*, 117501. [CrossRef]
7. Gomell, L.; Tsai, S.P.; Roscher, M.; Bueno Villoro, R.; Konijnenberg, P.; Zaefferer, S.; Scheu, C.; Gault, B. In situ nitriding of Fe 2 VAl during laser surface remelting to manipulate microstructure and crystalline defects. *Phys. Rev. Mater.* **2022**, *6*, 085405. [CrossRef]
8. Hargreaves, J.S.J. Heterogeneous catalysis with metal nitrides. *Coord. Chem. Rev.* **2013**, *257*, 2015–2031. [CrossRef]
9. Nagai, M. Transition-metal nitrides for hydrotreating catalyst—Synthesis, surface properties, and reactivities. *Appl. Catal. A Gen.* **2007**, *322*, 178–190. [CrossRef]
10. Furimsky, E. Metal carbides and nitrides as potential catalysts for hydroprocessing. *Appl. Catal. A Gen.* **2003**, *240*, 1–28. [CrossRef]
11. Bernard, P.; Stelmachowski, P.; Broś, P.; Makowski, W.; Kotarba, A. Demonstration of the Influence of Specific Surface Area on Reaction Rate in Heterogeneous Catalysis. *J. Chem. Educ.* **2021**, *98*, 935–940. [CrossRef]
12. Yuan, Y.; Adimi, S.; Guo, X.; Thomas, T.; Zhu, Y.; Guo, H.; Priyanga, G.S.; Yoo, P.; Wang, J.; Chen, J.; et al. A Surface-Oxide-Rich Activation Layer (SOAL) on Ni_2Mo_3N for a Rapid and Durable Oxygen Evolution Reaction. *Angew. Chem. Int. Ed.* **2020**, *59*, 18036–18041. [CrossRef]
13. Kakaei, K.; Esrafili, M.D.; Ehsani, A. Alcohol Oxidation and Hydrogen Evolution. In *Interface Science and Technology*; Kakaei, K., Esrafili, M.D., Ehsani, A., Eds.; Elsevier: Amsterdam, The Netherlands, 2019; Volume 27, pp. 253–301. [CrossRef]
14. Park, S.H.; Jo, T.H.; Lee, M.H.; Kawashima, K.; Mullins, C.B.; Lim, H.K.; Youn, D.H. Highly active and stable nickel–molybdenum nitride (Ni_2Mo_3N) electrocatalyst for hydrogen evolution. *J. Mater. Chem. A* **2021**, *9*, 4945–4951. [CrossRef]
15. Iffat, A.; Syed, R.; Mudassir, I. A Comprehensive Review on the Synthesis and Energy Applications of Nano-structured Metal Nitrides. *Front. Mater.* **2020**, *7*. [CrossRef]
16. Zhang, Y.; Ouyang, B.; Xu, J.; Chen, S.; Rawat, R.S.; Fan, H.J. 3D Porous Hierarchical Nickel-Molybdenum Nitrides Synthesized by RF Plasma as Highly Active and Stable Hydrogen-Evolution-Reaction Electrocatalysts. *Adv. Energy Mater.* **2016**, *6*, 1600221. [CrossRef]
17. Wise, R.S.; Markel, E.J. Catalytic NH_3 Decomposition by Topotactic Molybdenum Oxides and Nitrides: Effect on Temperature Programmed γ-Mo_2N Synthesis. *J. Catal.* **1994**, *145*, 335–343. [CrossRef]
18. Meuller, B.O.; Messing, M.E.; Engberg, D.L.J.; Jansson, A.M.; Johansson, L.I.M.; Norlén, S.M.; Tureson, N.; Deppert, K. Review of Spark Discharge Generators for Production of Nanoparticle Aerosols. *Aerosol Sci. Technol.* **2012**, *46*, 1256–1270. [CrossRef]
19. Hallberg, R.T.; Ludvigsson, L.; Preger, C.; Meuller, B.O.; Dick, K.A.; Messing, M.E. Hydrogen-assisted spark discharge generated metal nanoparticles to prevent oxide formation. *Aerosol Sci. Technol.* **2018**, *52*, 347–358. [CrossRef]
20. De la Peña, F.; Prestat, E.; Tonaas Fauske, V.; Burdet, P.; Jokubauskas, P.; Nord, M.; Furnival, T.; Ostasevicius, T.; MacArthur, K.E.; Johnstone, D.N.; et al. hyperspy/hyperspy: HyperSpy 1.6.0, version 1.6.0; Zenodo. 2020. Available online: https://zenodo.org/record/3973513#.Y9O-OHbMKUk (accessed on 6 December 2022).
21. Potapov, P.; Longo, P.; Okunishi, E. Enhancement of noisy EDX HRSTEM spectrum-images by combination of filtering and PCA. *Micron* **2017**, *96*, 29–37. [CrossRef] [PubMed]
22. Ritchie, N.W.M.; Newbury, D.E.; Davis, J.M. EDS Measurements of X-Ray Intensity at WDS Precision and Accuracy Using a Silicon Drift Detector Microscopy and Microanalysis. *Microsc. Microanal.* **2012**, *184*, 892–904. [CrossRef]
23. Newbury, D.E.; Ritchie, N.W.M. Performing elemental microanalysis with high accuracy and high precision by scanning electron microscopy/silicon drift detector energy-dispersive X-ray spectrometry (SEM/SDD-EDS). *J. Mater. Sci.* **2015**, *50*, 493–518. [CrossRef]

24. George, S.J.; Drury, O.B.; Fu, J.; Friedrich, S.; Doonan, C.J.; George, G.N.; White, J.M.; Young, C.G.; Cramer, S.P. Molybdenum X-ray absorption edges from 200 to 20,000eV: The benefits of soft X-ray spectroscopy for chemical speciation. *J. Inorg. Biochem.* **2009**, *103*, 157–167. [CrossRef]
25. Herle, P.S.; Hegde, M.S.; Sooryanarayana, K.; Guru Row, T.N.; Subbanna, G.N. Ni_2Mo_3N: A New Ternary Interstitial Nitride with a Filled β-Manganese Structure. *Inorg. Chem.* **1998**, *37*, 4128–4130. [CrossRef]
26. Conway, J.O.; Prior, T.J. Interstitial nitrides revisited—A simple synthesis of M_xMo_3N (M = Fe, Co, Ni). *J. Alloys Compd.* **2019**, *774*, 69–74. [CrossRef]
27. Cao, B.; Neuefeind, J.C.; Adzic, R.R.; Khalifah, P.G. Molybdenum nitrides as oxygen reduction reaction catalysts: Structural and electrochemical studies. *Inorg. Chem.* **2015**, *54*, 2128–2136. [CrossRef] [PubMed]
28. Bull, C.L.; McMillan, P.F.; Soignard, E.; Leinenweber, K. Determination of the crystal structure of delta-(Mo N) by neutron diffraction. *J. Solid State Chem.* **2004**, *177*, 1488–1492. [CrossRef]
29. Shoemaker, C.B.; Shoemaker, D.P. The crystal structure of the delta phase, Mo-Ni. *Acta Crystallogr.* **1963**, *16*, 997–1009. [CrossRef]
30. Straumanis, M.E.; Shodhan, R.P. Lattice parameter and thermal expansion coefficient of molybdenum between 15 and 65 C. *Trans. Metall. Soc. AIME* **1968**, *242*, 1185–1186.
31. Jette, E.; Foote, F. Precision determination of lattice constants. *J. Chem. Phys.* **1935**, *3*, 605–616. [CrossRef]
32. Tabrizi, N.S.; Xu, Q.; van der Pers, N.M.; Lafont, U.; Schmidt-Ott, A. Synthesis of mixed metallic nanoparticles by spark discharge. *J. Nanopart. Res.* **2009**, *11*, 1209–1218. [CrossRef]
33. Anastasopol, A.; Pfeiffer, T.V.; Middelkoop, J.; Lafont, U.; Canales-Perez, R.J.; Schmidt-Ott, A.; Mulder, F.M.; Eijt, S.W.H. Reduced enthalpy of metal hydride formation for MgTi nanocomposites produced by spark discharge generation. *J. Am. Chem. Soc.* **2013**, *135*, 7891–7900. [CrossRef]
34. Vons, V.A.; Leegwater, H.; Legerstee, W.J.; Eijt, S.W.H.; Schmidt-Ott, A. Hydrogen storage properties of spark generated palladium nanoparticles. *Int. J. Hydrog. Energy* **2010**, *35*, 5479–5489. [CrossRef]
35. Roth, C.; Ferron, G.A.; Karg, E.; Lentner, B.; Schumann, G.; Takenaka, S.; Heyder, J. Generation of ultrafine particles by spark discharging. *Aerosol Sci. Technol.* **2004**, *38*, 228–235. [CrossRef]
36. Vons, V.A.; Anastasopol, A.; Legerstee, W.J.; Mulder, F.M.; Eijt, S.W.H.; Schmidt-Ott, A. Low-temperature hydrogen desorption and the structural properties of spark discharge generated Mg nanoparticles. *Acta Mater.* **2011**, *59*, 3070–3080. [CrossRef]
37. Pfeiffer, T.V.; Feng, J.; Schmidt-Ott, A. New developments in spark production of nanoparticles. *Adv. Powder Technol.* **2014**, *25*, 56–70. [CrossRef]
38. Johnston, G.P.; Muenchausen, R.E.; Smith, D.M.; Foltyn, S.R. Reactive Laser Ablation Synthesis of Nanosize Aluminum Nitride. *J. Am. Ceram. Soc.* **1992**, *75*, 3465–3468. [CrossRef]
39. Luo, Q.; Congcong Lu, C.; Liu, L.; Zhu, M. A review on the synthesis of transition metal nitride nanostructures and their energy related applications. *Green Energy Environ.* 2022, *in press*. [CrossRef]
40. Duan, Y.; Wu, Y.; Zhang, O.; Ding, R.; Chen, Y.; Liu, J.; Yang, M. Towards conversion of octanoic acid to liquid hydrocarbon via hydrodeoxygenation over Mo promoter nickel-based catalyst. *J. Mol. Catal. A Chem.* **2015**, *398*, 72–78. [CrossRef]
41. Maluf, S.S.; Assaf, E.M. Ni catalysts with Mo promoter for methane steam reforming. *Fuel* **2009**, *88*, 1547–1553. [CrossRef]
42. Eijsbouts, S.; van den Oetelaar, L.C.A.; van Puijenbroek, R.R. MoS_2 morphology and promoter segregation in commercial Type 2 Ni–Mo/Al2O3 and Co–Mo/Al2O3 hydroprocessing catalysts. *J. Catal.* **2005**, *229*, 352–364. [CrossRef]